Stability-based transition model using transport equations

L. Pascal*, G. Delattre†, H. Deniau‡
ONERA/DMPE, Université de Toulouse - F-31055 Toulouse - France

J. Cliquet§
Airbus Opérations SAS - Toulouse - France

A laminar-turbulent transition model is presented. The model accounts for longitudinal transition mechanisms (i.e. Tollmien-Schlichting induced transition) and was calibrated using stability computations on similar boundary layer profiles at Mach number ranging from zero to four both on adiabatic and isothermal walls. The model embeds the so-called "C1-criterion" for transverse transition mechanisms (i.e. cross-flow waves induced transition).Finally, the model accounts for separation-induced transition by means of the Gleyzes criterion. The transition model is written under a transport equation formalism. Validations are performed on three-dimensional configurations and comparisons against results from a transition database method for natural transition, exact linear stability computations and experimental data are shown.

I. Nomenclature

α = Angle of attack

δ = Boundary layer thickness

δ_1 = Boundary layer displacement thickness

γ = Intermittency

β_0 = Angle between the wall friction vector and the velocity vector at the boundary layer edge

Λ_2 = Pohlhausen parameter $\Lambda_2 = \frac{\theta^2}{\nu_e}\frac{\mathrm{d}U_e}{\mathrm{d}s}$

ν = Kinematic viscosity

θ_1 = Boundary layer momentum thickness

H = Boundary layer shape factor $H = \delta_1/\theta_1$

$\widetilde{I}$ = Curvilinear coordinate measured from the transition location

M = Mach number

N = N factor of the envelope

Re_{δ_1} = Displacement thickness based Reynolds number

*Research Scientist, Multi-Physics and Energetics Department, lucas.pascal@onera.fr
†Research Scientist, Multi-Physics and Energetics Department
‡Research Scientist, Multi-Physics and Energetics Department
§Dr. Engineer

Re_{δ_2} = Transverse displacement thickness based Reynolds number

Re_θ = Momentum thickness based Reynolds number

s = Curvilinear coordinate

T_u = Turbulence intensity

$\underline{U}$ = Velocity vector field

y_n = Wall normal coordinate

Subscript

e = Boundary layer edge value

ϵ = Extracted around boundary layer edge using a blending function for added transported variables

i = Incompressible

cr = Critical point of the boundary layer

GL = Gleyzes criterion triggered

tr = Transition location

∞ = Free-stream

II. Introduction

Accurate computation of transport aircraft drag strongly relies on laminar-turbulent transition prediction capabilities. As Computational Fluid Dynamics (CFD) is now a major component of industrial processes, it is necessary to develop accurate transition prediction techniques for RANS solvers both for aerodynamic performance prediction and for design of future laminar transport aircraft concepts.

The development of transition prediction methods compatible with CFD is a major research topic. The notion of compatibility corresponds to the consistency in term of implementation with the global architecture of a CFD solver. A quite recent approach consists in using methods based on Partial Differential Equations (PDE). This approach consists in solving additional transport equations governing the dynamics of quantities that are related to a transition model. A very popular PDE-based method is the "$\gamma - Re_\theta$" approach of Langtry and Menter [1] based on phenomenological reasoning. This method has demonstrated success on many configurations and has been extended to handle cross-flow transition [2, 3] as well. The Amplification Factor Transport (AFT) method was derived more recently by Coder and Maughmer [4]. This promising method consists in writing under a transport equation the e^N-based approximate envelope method [5, 6] of Drela and Giles [7]. The AFT method was recently extended to include an intermittency variable [8] and cross-flow transition by Xu et al. [9]. The $\gamma - Re_\theta$ and AFT methods are said to be "local" in the sense that the additional transport equations associated to transition only involve values available at RANS computational

points. This property significantly reduces the implementation effort in a RANS solver. To do so the boundary layer variables required to trigger transition are obtained through correlations. As a consequence the application of the model may be restrained by the validity domain of the correlations considered.

In order not to rely on correlations accuracy and validity extent, boundary layer variables can be extracted from the flow thanks to wall-normal integration [10–12] and distributed to computational points via wall-normal communication. An accurate evaluation of the boundary layer integral quantities opens the way to other transition models such as the N-σ_P(NSP) model [13] based on the parabola method [14] and sensitive to small variations on integral quantities.

This paper presents a transport equation transition prediction and modeling approach incorporating the ONERA transition criteria (denoted AHD and C1). This paper is an extended version of the conference paper [14]. A similar method (restricted to the AHD and Gleyzes criteria) is proposed in Refs. [15, 16] where non local variables are approximated by means of local correlations. The transition criteria are presented in section III while section IV deals with their implementation in a RANS solver. Numerical results and validation are presented in section V.

III. Choice of the underlying transition criteria

Several physical mechanisms can lead to boundary layer transition. Each of them can be modeled individually by a dedicated criterion. Three different criteria have been selected and incorporated into the proposed model, taking advantage of their complementarity. The first one is the Arnal-Habiballah-Delcourt (AHD) criterion [17] derived for streamwise natural transition. The second one is the Gleyze criterion [18] for separation-induced transition. The third one is the C1 criterion [19, 20] for cross-flow induced transition. These criteria have already been detailed in the litterature, yet their expression are given again below to guide the reader through the modeling approach proposed.

A. AHD criterion

The Arnal-Habiballah-Delcourt (AHD) criterion [17] was derived by performing linear stability analysis on two-dimensional incompressible self-similar Falkner-Skan profiles. The criterion is given as a threshold on the momentum thickness Reynolds number and reads:

$$Re_{\theta,tr} = Re_{\theta,cr} + A(M_e)\exp(B(M_e,\bar{\Lambda}_2)\bar{\Lambda}_2)\left(\ln(C(M_e)T_u) - D(M_e)\bar{\Lambda}_2\right) \ . \tag{1}$$

where $Re_{\theta,cr}$ corresponds to the Reynolds number at the critical point which is defined as the location from which Tollmien-Schlichting waves are unstable and is given by:

$$Re_{\theta,cr} = \exp\left(G(M_e)/{H_i}^2 + E(M_e)/H_i - F(M_e)\right). \tag{2}$$

This value needs to be available downstream of the critical point so to evaluate the threshold value $Re_{\theta,tr}$ along the boundary layer. In the context of RANS solvers based on PDE, the idea of using a transport equation to have this value transported by the flow is quite natural.

The derivation of equation (1) and the coefficients are given in appendix A.

This criterion accounts for the flow history through $\bar{\Lambda}_2$ (spatial average of the Pohlhausen parameter), for receptivity through T_u and for compressibility through M_e. Another advantage of transport equations is their integration ability along streamlines. The spatial averaging can be done with two more transport equations: one for the integration of Λ_2 downstream of the critical point, and another for the integration of the curvilinear coordinate necessary for the averaging.

As this criterion is derived for natural transition, it should not be used for $T_u > 1\%$. Moreover, this criterion accounts for effects of wall temperature [21, section V].

B. Gleyzes criterion

Like the AHD criterion, Gleyzes criterion [18] was derived from linear stability computations on Falkner-Skan self-similar boundary layer profiles. However, Gleyzes et al. [18] considered separated boundary layer profiles and therefore the derived criterion is to be used to predict the transition onset in short laminar separation bubbles. This criterion assumes that in the neighbourhood of and within the separated region, the growth rate of Tollmien-Schlichting waves is almost independent of the frequency. Therefore $\frac{dN}{dRe_\theta}$ depends only on the incompressible shape factor and is expressed as:

$$\frac{dN}{dRe_\theta} = \frac{-2.4}{\mathcal{B}(H_i)} \tag{3}$$

The term $\mathcal{B}(H_i)$ is given in appendix B.

Since both the AHD criterion and the Gleyzes criteria are based on modeling $\mathrm{d}N/\mathrm{d}Re_\theta$, they can be combined to extend the range of application of the AHD criterion to separated flows [12]. In spite of the fact that the Gleyzes criterion was derived for incompressible flows, the combination of both criteria was successfully applied on compressible configurations [22–24].

Following the work of Cliquet et al. [12], the use of Gleyzes criterion is triggered when $H_i > 2.8$ in order to account for higher pressure gradient than can lead to flow separation. Let s_{GL} be the curvilinear coordinate from which the Gleyzes criterion is triggered. Likewise, N_{GL}, $\bar{\Lambda}_{2,GL}$ and $Re_{\theta,GL}$ correspond to values at s_{GL}. According to Eq. (3) The N-factor downstream of s_{GL} is simply:

$$N = N_{GL} + \int_{Re_{\theta,GL}}^{Re_\theta} \frac{-2.4}{\mathcal{B}(H_i)} \mathrm{d}R. \tag{4}$$

Let $\hat{N}$ be the N-factor according to the AHD criterion (see appendix A) corresponding to a fictitious flow where $\bar{\Lambda}_2$ remains $\bar{\Lambda}_{2,GL}$ downstream of s_{GL} ($\bar{\Lambda}_2 = \bar{\Lambda}_{2,GL}$ for $s \geq s_{GL}$):

$$\begin{aligned} \hat{N} &= a(\bar{\Lambda}_2)\left(Re_\theta - Re_{\theta,cr} + \Delta Re_{\theta,cr}(\bar{\Lambda}_2)\right) \\ &= N_{GL} + a(\bar{\Lambda}_{2,GL})(Re_\theta - Re_{\theta,GL}). \end{aligned} \tag{5}$$

Substituting N_{GL} from Eq. (5) into Eq. (4) yields:

$$N = a(\bar{\Lambda}_2)\left(Re_\theta - \hat{Re}_{\theta,cr} + \Delta Re_{\theta,cr}(\bar{\Lambda}_2)\right), \tag{6}$$

which corresponds to the standard form of the AHD criterion Eq. (22) (see appendix A) where the critical Reynolds number $Re_{\theta,cr}$ has been replaced by

$$\hat{Re}_{\theta,cr} = Re_{\theta,cr} + \int_{s_{GL}}^{s} \left(\frac{2.4}{a(\bar{\Lambda}_{2,GL})\mathcal{B}(H_i)} + 1\right)\frac{dRe_\theta}{ds}\mathrm{d}\xi \ . \tag{7}$$

.

Eq. (1) can then be applied by replacing $Re_{\theta,cr}$ by $\hat{Re}_{\theta,cr}$ to combine both AHD and Gleyzes criterion. The subsequent change on $Re_{\theta,tr}$ models the effect of higher pressure gradient and flow separation on boundary layer stability. The Gleyzes criterion can be introduced as a correction of the AHD criterion. In the proposed model it will be accounted for using the same transport equations as the AHD criterion.

Following Ref. [7], $\frac{dRe_\theta}{ds}$ can be approximated by the following correlation:

$$\frac{dRe_\theta}{ds} = \frac{1}{2\theta}\left(0.058\frac{(H_i-4)^2}{H_i-1} + \frac{6.54H_i - 14.07}{H_i^2} - 0.068\right) . \tag{8}$$

C. C1 criterion

The C1 criterion [19, 20] is used to predict natural transition induced by cross-flow instabilities. Contrary to the AHD criterion, the C1 criterion does not rely on linear stability computation but is based on wind tunnel experiments. Therefore, it embeds both steady and unsteady cross-flow waves. As a result, it might be too conservative when applied in flight conditions [25].

The criterion defines the transition point as the location where the transverse incompressible displacement thickness

Reynolds number $Re_{\delta_{2i}}$ equals a threshold given by:

$$Re_{\delta_2,i,tr} = \begin{cases} 150 & H_i \leq 2.31 \\ \frac{300}{\pi} \arctan\left(\frac{0.106}{(H_i - 2.3)^{2.052}}\right)\left(1 + \frac{\gamma - 1}{2} M_e^2\right) & 2.31 < H_i < 2.65 \end{cases} \tag{9}$$

The criterion should not be applied for $H_i > 2.65$. As this criteria does not require quantities to transport nor to integrate along the flow, no additionnal transport equation is needed to its incorporation in the model.

D. Parabola method as a reference

The so-called parabola method [26] is a database method which gives the growth-rate of longitudinal and transverse instabilities for a given velocity profile at a much lower computational effort than exact local linear stability analysis. Although this method is not incorporated in the proposed model, it was shown to agree well with exact local linear stability analysis [22, 26] and will therefore be considered as a reference for validation when experimental data is lacking.

As far as longitudinal instabilities are concerned, the growth rate of a wave is given as a function of the angle ϕ between the wave vector and the streamline at the boundary layer edge, its frequency f and the following parameters of the boundary layer profile: the displacement thickness δ_1, the unit boundary layer Reynolds number $Re^* = U_e/\nu_e$, the incompressible shape factor H_i and the Mach number at the edge of the boundary layer M_e.

In the model for travelling and stationary crossflow, the growth rate of a wave is given as a function of its angle ϕ, its frequency f (only for traveling crossflow instabilities) and the following quantities characteristic of the boundary layer profile: the displacement thickness δ_1, the transverse displacement thickness δ_2, the unitary Reynolds number and the characteristics of the generalized inflection point.

The NSP model [13] mentioned in the introduction is the implementation of this parabola method by means of transport equations.

IV. Building the transport equations

Evaluating eqs. (1) and (9) requires the knowledge of boundary layer variables Re_θ, Re_{δ_2}, M_e, etc .... As for approaches presented in Ref. [1] and [4], some of these variables can obtained through correlations to keep the model "local". For accuracy purpose, a prefered way is to compute these quantities through wall-normal integration. Moreover the proposed model takes advantages of wall-normal communication to store and call data shared by volume cells with common corresponding wall interface.

The detection of the leading edge stagnation line location is computed automatically by following the method proposed by Kenwright et al. [27] in order to perform specific operations in its neighborhood. This method, based on

phase plane analysis, only requires a local analysis of the friction vector field at the wall.

The proposed transition model is based on transport equations which ensures that transition criteria are evaluated along streamlines. The method shares similarities with the NSP transition model of Bégou et al. [13] [28] who proposed an implementation of the ONERA parabola method based on the equation transport concept as it enables either to transport or to integrate quantities along streamlines very easily. This previous modeling experience was of great help in the design of the proposed model. In the previous section, the incorporation of the AHD criterion in the model was shown to require the addition of three transport equations: one to transport the Reynolds number from critical point downwards the stream, and two more to integrate both the Pohlhausen parameter and the curvilinear asbscissa downstream of the critical point enabling the estimation of an averaged value of the Pohlhausen parameter. Both Gleyzes and C1 criteria were shown to be integrable with no need for more transport equations. If the three forementioned equation enable to evaluate the transition criteria along the flow, they will only allow to detect the transition onset location. The model will be completed by a fourth transport equation to account for the progressive rise of the intermittency downstream of the transition onset location.

A. Momentum-thickness Reynolds number

The first prerequisite to estimate the transition threshold $Re_{\theta,tr}$ following eq. (1) is to know the value of the critical Reynolds number. The latter corresponds to the value of Re_θ at the critical location (where Re_θ reaches $Re_{\theta,cr}$ given by Eq. (2)) of the current boundary layer edge streamline. We introduce variable $\widetilde{Re}_{\theta,cr}$ that will be transported by the flow to access to the needed value of $Re_{\theta,cr}$ by first writing the following evolution equation for $\widetilde{Re}_{\theta,cr}$:

$$\partial_t \left(\rho \widetilde{Re}_{\theta,cr}\right) + \nu_{cr} \nabla \cdot \left(\rho \widetilde{Re}_{\theta,cr} \underline{U}\right) = S_{Re_{\theta,cr}} \tag{10}$$

where ν_{cr} is a trigger defined for each cell depending on the state of the corresponding wall interface:

$$\nu_{cr} = \begin{cases} 0. \text{ if } Re_\theta < \widetilde{Re}_{\theta,cr,\epsilon} \\ 1. \text{ else} \end{cases} \tag{11}$$

and the source term:

$$S_{Re_{\theta,cr}} = \Gamma_{\widetilde{Re}_{\theta,cr}} (1 - \nu_{cr}) \Gamma_\delta \left(\widetilde{Re}_{\theta,cr} - Re_{\theta,cr}\right) \tag{12}$$

where $Re_{\theta,cr}$ is given by Eq. (2) and where Re_θ is computed following its exact definition by means of wall-normal integration. ν_{cr} equals zero at the leading edge attachment line and in the subcritical region defined as where

$Re_\theta < \widetilde{Re}_{\theta,cr,\epsilon}$. This boundary layer edge value $\widetilde{Re}_{\theta,cr,\epsilon}$ is obtained from the transported variable $\widetilde{Re}_{\theta,cr}$ using a pondering function defined at wall interfaces for any tranported variable $\widetilde{X}$ as:

$$\widetilde{X}_\epsilon = \frac{\sum \widetilde{X} w}{w} \qquad w = \left|\frac{\delta/A}{d^*}\right|^\alpha \qquad d^* = max\left(\frac{\delta}{A}, |y_m - \delta|\right) \tag{13}$$

with constant A and α arbitrarily set to 10. and 4. respectively. As the function $\widetilde{X}_\epsilon$ is defined at wall interfaces, the sum in the first equation is performed on all cells associated to a given wall interface.

In the region downstream of the critical point, defined as $Re_\theta \geq \widetilde{Re}_{\theta,cr,\epsilon}$, the trigger ν_{cr} is set to one. As a consequence, as long as the boundary layer is not critical ($\nu_{cr} = 0$) the source term forces $\widetilde{Re}_{\theta,cr}$ to equal $Re_{\theta,cr}$ with help of a parameter $\Gamma_{\widetilde{Re}_{\theta,cr}}$ typically set to 1.1 for stationary flow convergence speed up. If the boundary layer becomes critical ($\nu_{cr} = 1$) $\widetilde{Re}_{\theta,cr}$ is simply convected. The source term impact is limited to an area surrounding the wall by Γ_δ defined by:

$$\Gamma_\delta = \exp\left(-\left(\frac{y_n}{4\delta}\right)^4\right). \tag{14}$$

To account for the Gleyzes criterion for separation induced transition, $S_{Re_{\theta,cr}}$ is completed with another source term triggered by ν_{GL}. Eq. (12) is modified:

$$S_{Re_{\theta,cr}} = \Gamma_{\widetilde{Re}_{\theta,cr}}(1-\nu_{cr})\Gamma_\delta\left(\widetilde{Re}_{\theta,cr} - Re_{\theta,cr}\right) + \nu_{GL}\Gamma_\delta\rho||U||\left(\frac{2.4}{a(\tilde{\bar{\Lambda}}_2)\mathcal{B}(H_i)} + 1\right)\frac{dRe_\theta}{ds}\,. \tag{15}$$

Following the work of Cliquet et al. [12], ν_{GL} is set to one if $H_i > 2.8$. Moreover, it is here chosen to set ν_{GL} to one if $\beta_0 > \pi/2$, which is a condition sufficient for a boundary layer profile to be separated. $\frac{dRe_\theta}{ds}$ is given by Eq. (8).

Although it might be already the case, ν_{cr} is set to one if ν_{GL} equals one.

B. Pohlhausen parameter averaging

The second prerequisite to compute the transition threshold $Re_\theta > Re_{\theta,tr}$ following eq. (1) is to compute the value of $\bar{\Lambda}_2$. As the variable $\bar{\Lambda}_2$ corresponds to an integration performed along the streamline at the boundary layer edge, a transport equation is introduced for a variable $\tilde{\bar{\Lambda}}_2$ and another for a variable $\tilde{s}$:

$$\partial_t\left(\rho\tilde{\bar{\Lambda}}_2\right) + \nabla\cdot\left(\rho\tilde{\bar{\Lambda}}_2\underline{U}\right) = \nu_{cr}\Gamma_\delta\frac{\rho||\underline{U}||}{\tilde{s}}\left(\Lambda_2 - \tilde{\bar{\Lambda}}_2\right) + \Gamma_{\tilde{\bar{\Lambda}}_2}(1-\nu_{cr})\Gamma_\delta\rho(\tilde{\bar{\Lambda}}_2 - \Lambda_2)\,. \tag{16}$$

$$\partial_t(\rho\tilde{s}) + \nabla\cdot\left(\rho\tilde{s}\underline{U}\right) = \nu_{cr}\Gamma_\delta\rho||\underline{U}|| - \Gamma_s\rho(1-\nu_{cr})\,\tilde{s}\,. \tag{17}$$

where $\tilde{s}$ corresponds to the curvilinear coordinate measured from the critical point. Upstream of the critical location ($\nu_{cr} = 0$), the second terms of the right-hand side of Eq. (16) and (17) act as forcing terms toward the local value of the Pohlhausen parameter Λ_2 and to zero respectively. This enables to start the integration of the Pohlhausen parameter from its value at the critical point on the one hand, and to start from zero the curvilinear coordinate from this same location on the other hand. Both conditions are necessary to estimate properly the averaged Pohlhausen parameter over the critical region. The boundary layer shielding is made using Γ_δ. Parameters $\Gamma_{\widetilde{\bar{\Lambda}}_2}$ and Γ_s are set to 1.1 for the same reasons as for $\Gamma_{\widetilde{Re}_{\theta,cr}}$. Downstream of the critical location ($\nu_{cr} = 1$), the first terms of the right hand sides of Eq. (16) and (17) correspond to the integration of Λ_2 along a streamline (see appendix C.2 for the mathematical proof) and the integration of a curvilinear coordinate along the same path (see the mathematical proof in appendix C.1) from the critical point.

To account for the Gleyzes criterion, these equations have to be modified to ensure that $\bar{\Lambda}_2$ keeps the value of $\bar{\Lambda}_{2,GL}$ downstream of s_{GL} (see section III.B). This is done with the trigger ν_{GL} to activate the Gleyzes criterion by adding $(1 - \nu_{GL})$ in factor of the first terms of the right-hand side of Eq. (16) and (17):

$$\partial_t \left(\rho\widetilde{\bar{\Lambda}}_2\right) + \nabla \cdot \left(\rho\widetilde{\bar{\Lambda}}_2\underline{U}\right) = \nu_{cr}(1-\nu_{GL})\Gamma_\delta \frac{\rho||\underline{U}||}{\tilde{s}} \left(\Lambda_2 - \widetilde{\bar{\Lambda}}_2\right) + \Gamma_{\widetilde{\bar{\Lambda}}_2}(1-\nu_{cr})\Gamma_\delta\rho(\widetilde{\bar{\Lambda}}_2 - \Lambda_2)\,. \tag{18}$$

$$\partial_t \left(\rho\tilde{s}\right) + \nabla \cdot \left(\rho\tilde{s}\underline{U}\right) = \nu_{cr}(1-\nu_{GL})\Gamma_\delta\rho||\underline{U}|| - \Gamma_s\rho\left(1-\nu_{cr}\right)\tilde{s}\,. \tag{19}$$

C. C1 criterion and transition onset

The transition threshold on Re_θ given by Eq. (1) can then be evaluated from $\widetilde{\bar{\Lambda}}_{2,\epsilon}$ and $\widetilde{Re}_{\theta,cr,\epsilon}$ obtained by extracting $\widetilde{\bar{\Lambda}}_2$ and $\widetilde{Re}_{\theta,cr}$ at the edge of the boundary layer (see Eq. (13)) since the AHD criterion is to be evaluated along streamlines at the boundary layer edge. A new trigger ν_{tr} is used for transition onset. Its value is set to zero at the leading edge and as long as the transition threshold of the AHD criterion Eq. (1) is not reached. If the transition threshold is reached, ν_{tr} is set to one. Due to the simplicity of the C1 criterion, its implementation is quite straightforward. It consists in setting ν_{tr} to one if $Re_{\delta_{2,i}}$ reaches the threshold given by Eq. (9).

D. Intermittency raise and coupling with turbulence models

Finally, a last equation is added to transport downstream the information that transition has been triggered. It is chosen to introduce a new variable $\widetilde{I}$ that corresponds to the curvilinear coordinate measured from the transition point. The purpose of this curvilinear coordinate is to be able to control the extent of the transition region and the raise of an

intermittency fuction over this region. Variable $\widetilde{I}$ is governed by the following transport equation:

$$\partial_t \left(\rho\widetilde{I}\right) + \nabla \cdot \left(\rho\widetilde{I}\underline{U}\right) = \nu_{tr}\Gamma_\delta \rho ||\underline{U}|| - \Gamma_I \rho \left(1 - \nu_{tr}\right)\widetilde{I} \ . \tag{20}$$

Eq. (20) is very similar to Eq. (17) where ν_{cr} is replaced by ν_{tr}. Thus, while $\tilde{s}$ is the curvilinear coordinate measured along a streamline from the critical location, $\tilde{I}$ is the curvilinear coordinate measured along a streamline from the transition onset location. The intermittency is evaluated from the value of $\widetilde{I}$ at the boundary layer edge $\widetilde{I}_\epsilon$ according to:

$$\gamma(\widetilde{I}_\epsilon) = 1 - \exp\left(-5\left(\frac{\widetilde{I}_\epsilon}{l_{tr}}\right)^2\right). \tag{21}$$

Eq. (21) is derived from Ref. [29, Eqs. (1,6)].

In the current implementation, the intermittency is defined at a wall interface and set constant in the whole boundary layer profile by means of wall normal communication.

The coupling with the turbulence model such as Spalart and Allmaras [30] and Menter [31] consists in multiplying the Reynolds stress tensor by the intermittency in momentum equations of the mean flow. The production term of the turbulence model of Spalart and Allmaras and the production on the ω-equation of the Menter turbulence model are multiplied by the intermittency.

At the current stage of development, the streamwise length l_{tr} of the transition region is implemented as a user input. Choosing a too short length might result in convergence issues [29]. l_{tr} can be chosen from a priori knowledge or can be manually computed from correlations, see for instance Ref. [29]. On going developments aim at implementing such correlations in order to remove this user-dependent modeling parameter.

V. Validations

The proposed transition model has been implemented in the *elsA* [32] CFD software. The latter solves the compressible 3D Navier-Stokes equations on multi-block structured meshes. Cell-centered finite volume method is used to solve the system of equations. Both upwind and classical second order spatial discretization schemes are available. Implicit backward Euler technique is usually used for time integration. The *elsA* software features a large number of turbulence models.

Evaluating eqs. (1) and (9) requires the knowledge of boundary layer variables Re_θ, Re_{δ_2}, M_e, etc .... Contrary to the approaches presented in Ref. [1] and [4], the present implementation does not rely on correlations based on local variables. Non local variables are evaluated and made available at each cell point in *elsA* thanks to the fact that it is possible to: i) get for a cell in the volume the associated wall interface (if there is any) and ii) know which cells in the volume form the mesh line normal to a given wall interface. Therefore, it is then possible to access the

flow profile along the wall normal and compute the boundary layer thickness δ [12, section II-B], the boundary layer integral quantities (e.g. δ_1, θ) by wall-normal integration and the values at the boundary layer edge (e.g M_e, ν_e) by interpolating a quantity at $y_n = \delta$.

Two three dimensional configurations have been chosen to validate the prediction method. *elsA* computations are performed with a second order Roe spatial scheme and a backward Euler time scheme. In the following, only the Menter-SST turbulence model [31] is used.

In the following, "transition line" denotes the location where the intermittency γ starts to grow.

A. Nacelle transition prediction

While numerical validations of transition models in CFD are usually made on wings, numerical results on the XRF1 nacelle configuration of Airbus are shown in this section. XRF1 is a test case provided by Airbus to collaborate with external partners. A cut view of the geometry and of the surface mesh is shown in Fig. 1. In the following, for the sake of visibility, both sides are "unrolled": the contours are shown in a plane (x, ψ) where $\psi \in [0, 2\pi]$ is defined as $\tan(\psi) = z/y$ (see Fig. 1 for the definition of the mesh axes).

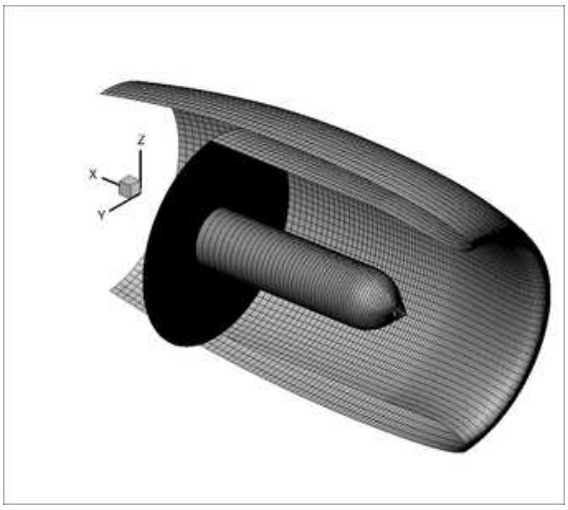

Fig. 1 Cut view of the XRF1 nacelle (mesh #1). Pressure boundary condition is imposed on the black surface.

Computations were performed on four meshes in order to evaluate the grid convergence. The approximate number of cells contained in the boundary layer thickness in the laminar region is given in Tab. 1 together with the number of elements along the chord and the total number of cells in the whole mesh. The four meshes were built with 100 elements in the azimuthal direction.

The turbulence level is set to $T_u = 0.1\%$. This value corresponds to the upper bound of the turbulence level in flight conditions. The flow conditions are imposed with $\alpha = 1.1^{\circ}$ and M_∞=0.6. The transition length l_{tr} is set to 5%

Table 1 XRF1 nacelle - Mesh refinement

	Number of cells		
	In the boundary layer thickness (laminar)	In the streamwise direction	In the whole mesh
Mesh #1	10-20	120	3×10^6
Mesh #2	40-60	120	4.9×10^6
Mesh #3	60-80	120	6.5×10^6
Mesh #4	60-80	226	12.1×10^6

of the nacelle length.

1. Grid convergence study

Figures 2(a,b) show the transition lines computed for the four meshes on both sides. The transition lines computed for mesh #2, #3 and #4 agree very well. A slight deviation is observed on the inner side near $\psi = 0$ and $\psi = \pi$ (these two regions are further investigated in the next section). The transition lines computed for the mesh #1 agree quite well except on the upper part of the outer side and near $\psi = 0$ and $\psi = \pi$ on the inner side.

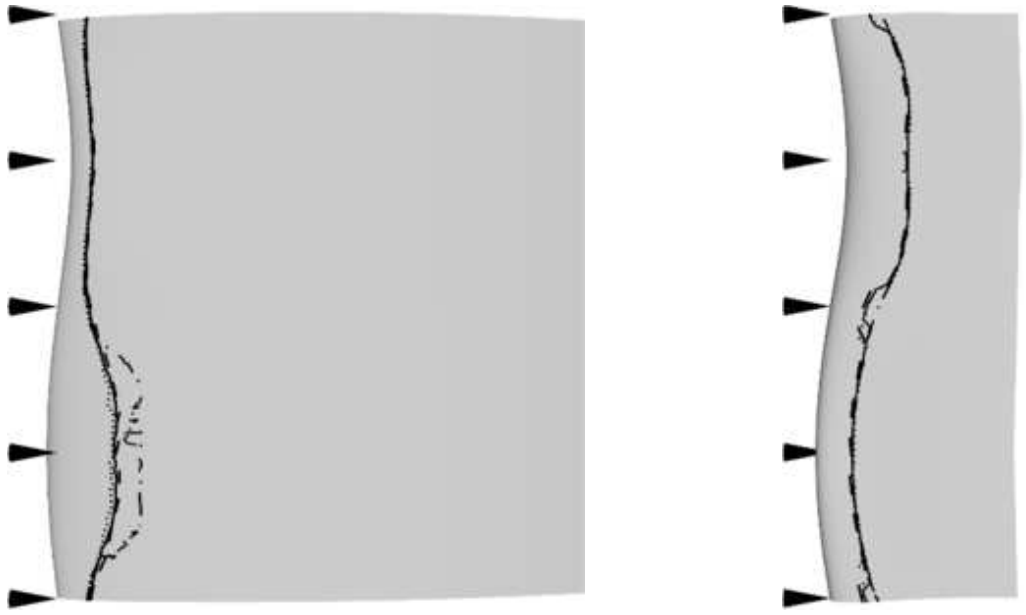

(a) (b)

Fig. 2 Transition line computed on mesh #1 (dash-dotted line), mesh #2 (dotted line), mesh #3 (dashed line) and mesh #4 (solid line) at the outer (a) and inner (b) sides of the nacelle. Black cones depict $\psi \in \{0, \pi/2, \pi, 3\pi/2, 2\pi\}$. The flow goes from left to right.

2. Validation of the implementation by means of transport equations

As no experimental results are available on this geometry, comparisons are made against results obtained by means of the boundary layer equations solver `3C3D` [33]. The latter requires as input the velocity at the edge of the boundary

layer, extracted here from a full turbulent computation performed with *elsA* on mesh #4. In 3C3D, transition is accounted for by means of the parabola method both for longitudinal and crossflow transition. The N-factor transition threshold $N_{CF,tr} = 7$ has been arbitrarily chosen for cross-flow transition. This value is comparable to the value chosen for instance by Kruse et al. [34] and $N_{TS,tr}$ is deduced from the turbulence level using Mack's law [35]. Moreover, a full laminar computation is performed with 3C3D. Exact local linear stability computations are then performed on the obtained boundary layer profiles at $\psi = \{0, \pi/2, \pi, 3\pi/2\}$ both at the inner and outer sides.

Comparison between the *elsA* computation, the 3C3D computation and exact local linear stability analysis is plotted on Figs. 3(a,b) on the outer and inner sides of the nacelle. As expected from the authors experience, the parabola method agrees very well with exact local linear stability analysis both at the inner and outer side. According to the parabola method and exact local linear stability analysis, transition is only triggered by Tollmien-Schlichting waves.

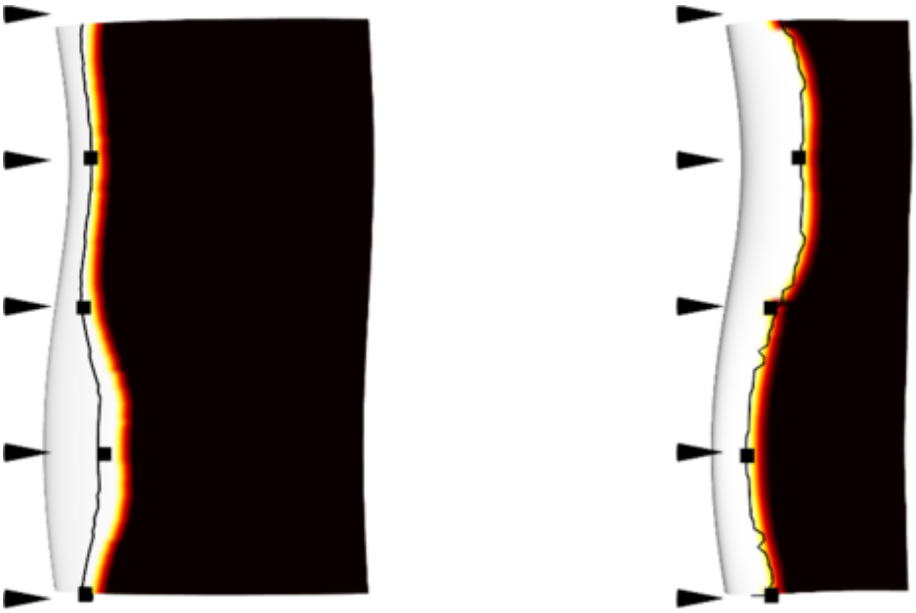

(a) (b)

Fig. 3 Intermittency contours computed on mesh #4 with *elsA* by means of the AHD and C1 criteria for transition prediction (light and dark shading corresponds respectively to $\gamma = 0$ and $\gamma = 1$) at the outer (a) and inner (b) sides of the nacelle. The black line depicts the transition location predicted by 3C3D and the black squares correspond to exact linear stability computations. Black cones depict $\psi \in \{0, \pi/2, \pi, 3\pi/2, 2\pi\}$. The flow goes from left to right.

The model proposed in this paper gives a transition line in good agreement with the parabola method on both inner and outer sides.

Transition is mostly triggered by the AHD criterion. The C1 transition threshold is reached only in two small regions near $\psi = 0$ and $\psi = \pi$. Since the angle of attack is non-zero, a locally higher cross-flow velocity component is here expected. Figure 4(a) (respectively 4(b)) shows a zoom of extent $\pi/6$ near the transition line at $\psi = 0$ (respectively $\psi = \pi$). The circles depict the locations where the C1 transition threshold is reached. The squares depict the most

upstream location where the AHD transition threshold is reached (downstream of this location, Re_θ is everywhere greater than this threshold). The scenario observed is quite pathological in the sense that the C1 transition threshold is only locally reached and transition is not fully triggered by the C1 criterion. The cross-flow N-factor computed by means of the parabola method goes up to 5 in this region (not shown in the paper). This indicates that cross-flow waves are indeed unstable but their amplification remains too low to trigger transition. This deviation between the parabola method and the C1 criterion can be explained by the fact that the latter is based on wind-tunnel measurements and may in some cases be too conservative [25].

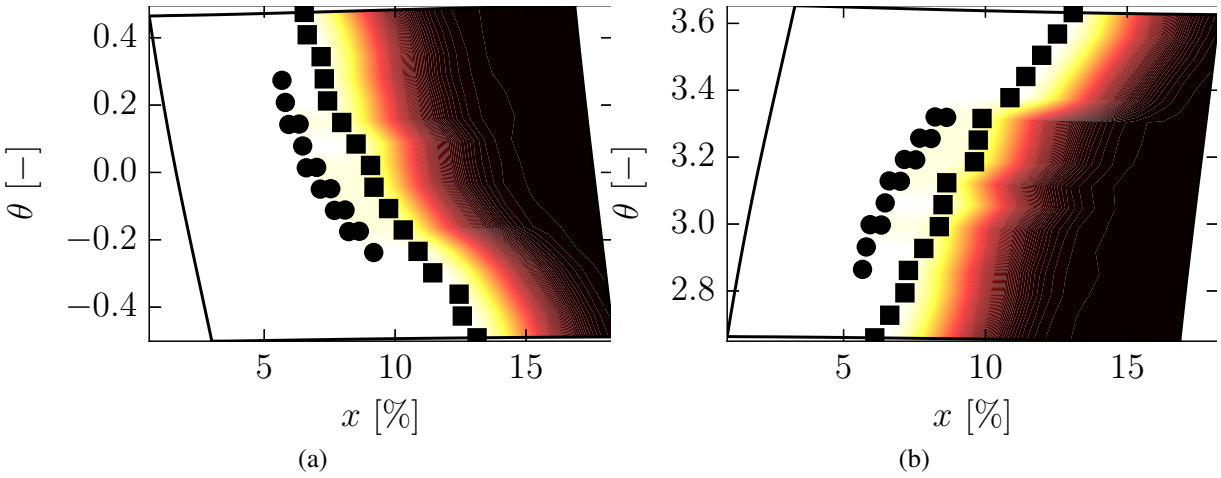

Fig. 4 Intermittency contours computed on mesh #4 with *elsA* by means of the AHD and C1 criteria for transition prediction (light and dark shading corresponds respectively to $\gamma = 0$ and $\gamma = 1$) near $\psi = 0$ (a) and $\psi = \pi$(b) on the inner side of the nacelle. The flow goes from left to right.

3. Langtry-Menter transition model

For the sake of comparison, the results obtained with the transition model of Langtry and Menter [1] (without crossflow extension [2]) are plotted on Fig. 5 for mesh #2. Contours of incompressible shape factor are plotted, turbulent flow corresponds here to $H_i \approx 1.5$ and laminar flow to $H_i >\sim 2.2$. Contrary to the results obtained with the proposed model, the intermittency γ is not directly available with the $\gamma - Re_\theta$ model. Therefore the incompressible shape factor has been chosen to indicate the transition onset. In order to validate this choice of transition onset indicator, the incompressible shape factor contours obtained with the proposed model is plotted figure 6.

Langtry-Menter model agrees fairly well with the parabola method even though it systematically precedes the transition location, especially for $\psi \approx \pi/2$ at both the inner and outer sides. In these two regions, the pressure gradient is favorable and therefore the Langtry-Menter model is likely to underestimate $Re_{\theta,t}$ [36].

In order to compare more in details the proposed model and the Langtry-Menter model, the log files of about fifty computations on mesh #2 for each model have been post-processed. The computation time per iteration is found to be 1.43 higher with the proposed model. This value is comparable to the ratio of the number of equations to solve

$11/9 = 1.22$ The ratio of the total memory allocated is 110% higher with the proposed model.

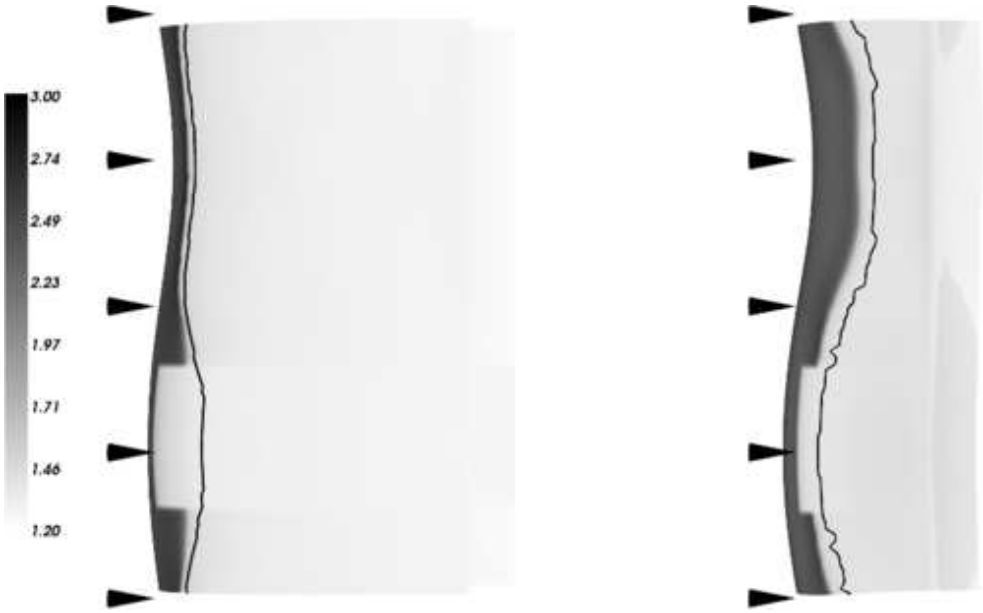

(a) (b)

Fig. 5 Incompressible shape factor H_i contours computed with *elsA* by means of the Langtry-Menter model for transition prediction at the outer (a) and inner (b) sides of the nacelle. The solid line depicts the transition location predicted by 3C3D by means of the parabola method. Black cones depict $\psi \in \{0, \pi/2, \pi, 3\pi/2, 2\pi\}$. The flow goes from left to right.

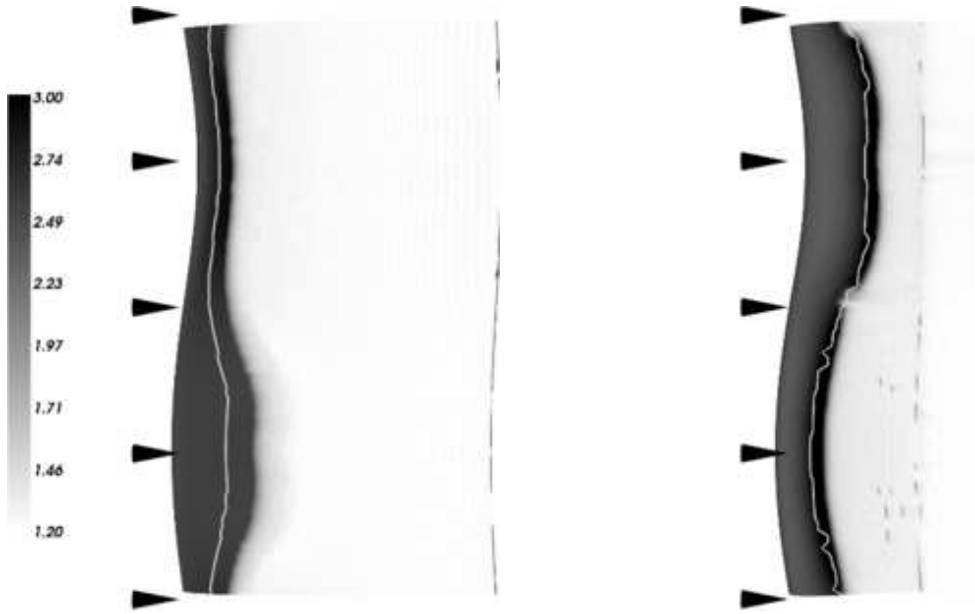

(a) (b)

Fig. 6 Incompressible shape factor H_i contours computed with *elsA* by means of the AHD and C1 criteria for transition prediction at the outer (a) and inner (b) sides of the nacelle. The solid line depicts the transition location predicted by 3C3D by means of the parabola method. Black cones depict $\psi \in \{0, \pi/2, \pi, 3\pi/2, 2\pi\}$. The flow goes from left to right.

Table 2 Flow cases

	Re	α
Case A	2.75×10^6	-2.6^o
Case B	4.5×10^6	-2.6^o
Case C	4.5×10^6	-0.3^o
Case D	2.75×10^6	6.0^o

B. TU Braunschweig Sickle Wing

The last validation case is the TU Braunschweig Sickle Wing [34, 37]. This configuration is an interesting validation case since "the sickle-shaped planform with distinct kinks creates spanwise gradients, and the assumptions of linear local stability theory are therefore challenged" [37]. Kruse et al. [34] measured the transition location by means of infrared thermography.

Computations are performed for the four flow cases defined and made available for the "AIAA Applied Aerodynamics CFD Transition Modeling and Predictive Capabilities Special Session" held at the AIAA SciTech 2018, see Table 2. Transition line prediction by means of linear stability analysis was given by Kruse et al. [34] for all four cases and on both sides. They found overall good agreement with the experimental results.

An overset technique is used to mesh the wing within the wind tunnel. The mesh contains 48×10^6 cells among which 5.7×10^6 are in the overset block containing the wing. The latter is meshed with 230 elements along the chord on each side. The unswept segment at the root is meshed with 60 elements along the span while each swept segment is meshed with 120 elements along the span. The transition length l_{tr} is set to 10% of the wing reference chord length. For all four cases, between 40 and 60 cells are contained within the boundary layer thickness. For all four computations, the flow is forced to be turbulent at the root of the wing on both sides as in Ref. [34]. In the experiments, this region is expected to be turbulent because of the contamination from the turbulent flow on the wind tunnel wall.

The computed intermittency is plotted on Figures 7, 8, 9 and 10 together with the experimentally measured transition locations.

For case A (Figure 7), very good agreement is obtained on the pressure side, where transition is exclusively triggered by the combination of the AHD and Gleyzes criteria except at the kinks where transition is triggered by the C1 criterion.

As far as the suction side is concerned, transition is triggered by the C1 criterion between the two dashed line, elsewhere the combination of the AHD and Gleyzes criteria triggers transition. Overall, the model agrees well with the experiments. Near sections A and B and above section C, the model is not able to reproduce the experimental results. However, the computed transition line near section B and at the tip agrees qualitatively well with the exact linear stability computations performed by Kruse et al. [34].

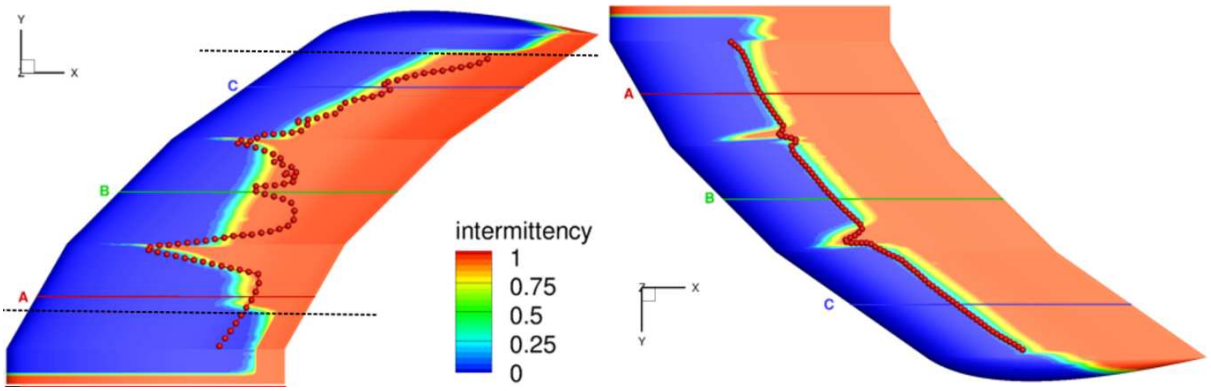

Fig. 7 TU Braunschweig Sickle Wing, case A - Contours of γ compared to the experimentally measured transition locations at the suction (left) and pressure (right) sides.

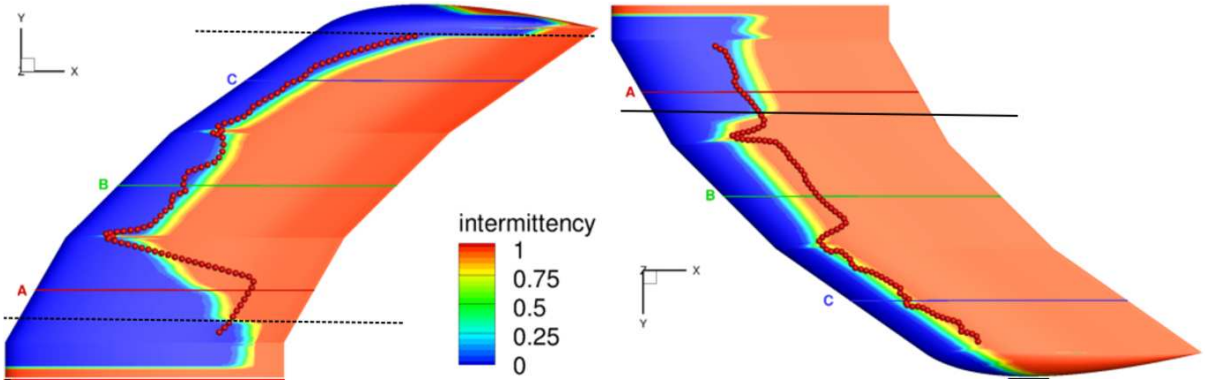

Fig. 8 TU Braunschweig Sickle Wing, case B - Contours of γ compared to the experimentally measured transition locations at the suction (left) and pressure (right) sides.

In case B (Figure 8), the C1 criterion triggers transition between the two dashed curve on the upper side and above the solid line on the pressure side. Elsewhere, the transition is triggered by the combination of the AHD and Gleyzes criteria. The computed transition location agrees quite well with the experiments. On the pressure at section B, the transition line computed by the proposed model is slightly too far upstream compared to the experiments and the linear stability computation of Kruse et al. [34, Figure 11].

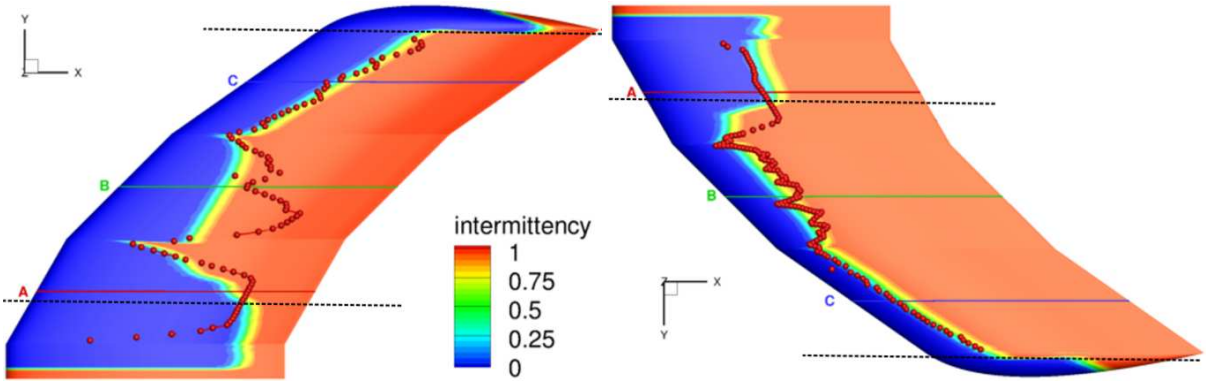

Fig. 9 TU Braunschweig Sickle Wing, case C - Contours of γ compared to the experimentally measured transition locations at the suction (left) and pressure (right) sides.

As far as case C is concerned, the transition onset is due to the C1 criterion between the two dashed lines while elsewhere the transition onset is due to the combination of AHD and Gleyzes criteria on both sides. The model yields quite good agreement with the experiments. As observed already in case A, the model is not able to reproduce the trend measured experimentally and computed by means of linear stability analysis by Kruse et al. [34] on the suction side near the span section B.

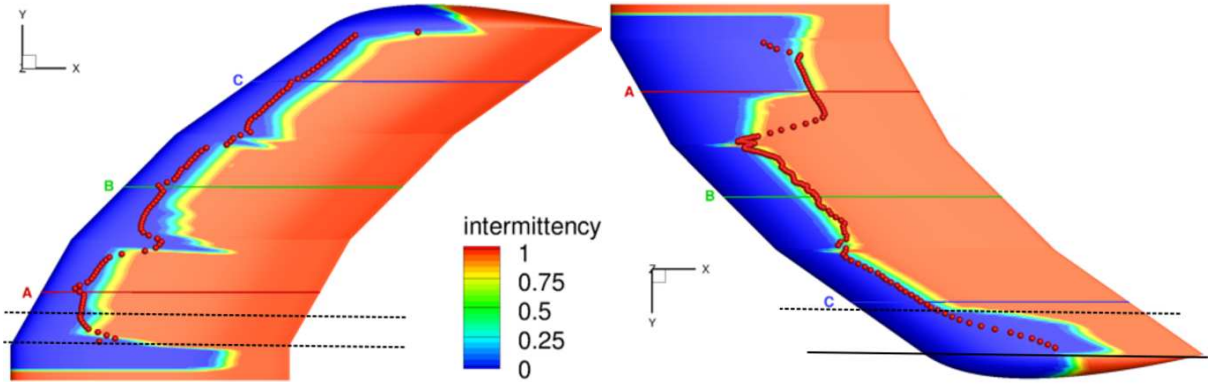

Fig. 10 TU Braunschweig Sickle Wing, case D - Contours of γ compared to the experimentally measured transition locations at the suction (left) and pressure (right) sides.

The transition model yields a quite good agreement with the experiments in case D (see Figure 10). Compared to the experiments, the model slightly delays the transition onset location on the suction side, especially near the first kink. Above the span section C on the pressure side, the model does not agree very well with the transition location

experimentally measured but is qualitatively in good agreement with the transition line predicted by means of linear stability computation [34, Figure 13]. Transition is here triggered by the C1 criterion between the two dashed lines on the suction side and between section A and the dashed line and above the solid line on the lower side. Everywhere else, transition is triggered by the combination of the AHD and Gleyzes criteria.

VI. Conclusion

An implementation of the stability based AHD criterion by means of transport equations is presented. This criterion, valid for Mach number up to $M = 4$ and for heated and cold wall, is combined with the C1 and Gleyzes criteria to account for cross-flow transition and transition in separation bubbles.

The implementation by means of transport equations and the accuracy of the model were validated for $M \leq 0.6$ by comparing with results obtained by means of both approximated and exact linear stability analysis on the XRF1 nacelle. Comparisons with the experiments were performed for four flow cases on the TU Braunschweig Sickle Wing geometry. The obtained results ranged from good to excellent agreement with the experiments.

Compared to the transition model of Langtry and Menter [1], the proposed model is more expensive on a numerical point of view as more transport equations have to be solved and wall normal communication is required. However, those additional equations were introduced in order to embed more physics and therefore the proposed model may be applied on a wider range of Mach number. If even higher accuracy is required and having a higher computational cost is affordable, the method of Bégou et al. [13] can be used since this method gives a close matching to exact linear stability computations. The method of Bégou et al. [13] complements well with the method presented in this paper as it can be used in more advanced design stages.

Acknowledgement

Andreas Krumbein (DLR Göttingen) and Martin Kruse (DLR Braunschweig) are gratefully acknowledged for providing the TU Braunschweig Sickle Wing CAD geometry and the experimentally measured transition locations.

elsA CFD software is property of ONERA-Airbus-Safran.

Appendix

A. AHD criterion

As explained in Ref. [38], the N-factor envelope is approximated by linear functions of the momentum based Reynolds number Re_θ where the two coefficients of the linear approximation depends on the Pohlhausen parameter $\Lambda_2 = \theta^2/\nu_e \frac{\mathrm{d}U_e}{\mathrm{d}s}$:

$$N = a(\Lambda_2)(Re_\theta - Re_{\theta,cr}(\Lambda_2) + \Delta Re_{\theta,cr}(\Lambda_2)) \tag{22}$$

where:

$$\begin{cases} a(\Lambda_2) = \dfrac{2.4}{A}\exp(-B\Lambda_2) \\ \Delta Re_{\theta,cr} = -\dfrac{2.4}{a(\Lambda_2)}\left(\dfrac{8.43}{2.4} - \log(C) + D\Lambda_2\right) \\ Re_{\theta,cr} = \exp\left(E/H_i - F\right) \end{cases} \tag{23}$$

with $A = -206$, $B = 25.7$, $C = 16.8$, $D = 2.77$, $E = 52$ and $F = 14.8$. $Re_{\theta,cr}$ is the Reynolds number at the critical point, i.e. the location from which Tollmien-Schlichting instabilities start to grow. The dependency on Λ_2 is replaced by a dependency on H_i as there exists a bijective relationship between both. $\Delta Re_{\theta,cr} < 0$ corresponds to an approximation error.

To apply Eq. (22) on spatially evolving flows, Λ_2 is replaced by $\bar{\Lambda}_2$ which corresponds to its averaged value between the critical point of curvilinear coordinate s_{cr} and the current location of curvilinear coordinate s (measured along the streamline at the edge of the boundary layer):

$$\bar{\Lambda}_2 = \frac{1}{s - s_{cr}}\int_{s_{cr}}^{s} \Lambda_2(\xi)\mathrm{d}\xi.$$

By combining Eqs. (22) and the transition threshold N_T given by the Mack's law [35] ($N_T = -2.4\ln(T_u) - 8.43$), the AHD transition criterion can be expressed as a threshold on Re_θ:

$$Re_{\theta,tr} = Re_{\theta,cr} + A\exp(B\bar{\Lambda}_2)\left(\ln(CT_u) - D\bar{\Lambda}_2\right) \ . \tag{24}$$

In its compressible extension [21], the variables A, B, C, D, E and F are functions of M_e, B depends as well on $\bar{\Lambda}_2$ and $Re_{theta,cr}$ depends on an additional coefficient G:

$$Re_{\theta,cr} = \exp\left(G(M_e)/{H_i}^2 + E(M_e)/H_i - F(M_e)\right).$$

The coefficients are given below:

$$A(M_e) = \begin{cases} -236.7 + M_e(117.16 + M_e(-356.47 + 98.65M_e)) \text{ if } M_e \leq 1.8 \\ 2582 + M_e(-3911 + M_e(1527 - 188M_e)) \text{ if } 1.8 < M_e \leq 2.8 \\ -2558 + M_e(1644 + M_e(-431.4 + 37.36M_e)) \text{ if } 2.8 < M_e \leq 4 \end{cases}$$

$$B(M_e, \bar{\Lambda}_2) = 22.04 + M_e(9.8252 + M_e(-3.0243 + 0.2952M_e)) + \bar{\Lambda}_2 B2(M_e, \bar{\Lambda}_2)$$

where if $\Lambda_2 \leq -0.0001$

$$B2(M_e, \bar{\Lambda}_2) = \begin{cases} -111.54 + M_e(284.73 + M_e(504.39 + M_e(-1175 + M_e(653.79 - 112.94M_e)))) \text{ if } M_e \leq 2.5 \\ -9626.3 + M_e(7357.6 + M_e(-1841.4 + 169.25M_e)) \text{ if } 2.5 < M_e \leq 4 \end{cases}$$

and else

$$B2(M_e, \bar{\Lambda}_2) = \begin{cases} -113.4 + M_e(17.47 + M_e(279.45 - 26.73M_e)) \text{ if } M_e \leq 3 \\ 1614.1 + M_e(1730 - 565.02M_e) \text{ if } 3 < M_e \leq 4 \end{cases}$$

$$C(M_e) = \begin{cases} 22.56 + M_e(-6.096 + M_e(31.2 + M_e(-54.63 + M_e(49.54 + M_e(-19.72 + 2.749M_e))))) \text{ if } M_e \leq 2.5 \\ 273.7 + M_e(-206 + M_e(55.76 - 4.99M_e)) \text{ if } 2.5 < M_e \leq 4 \end{cases}$$

$$D(M_e) = 12 - 0.5M_e$$

$$E(M_e) = \begin{cases} 51.904 + M_e(0.167 + M_e(-0.7379 + 0.6711M_e)) \text{ if } M_e \leq 1.1 \\ -641.04 + M_e(313.04 - 40.471M_e) \text{ if } 1.1 < M_e \leq 4 \end{cases}$$

$$F(M_e) = \begin{cases} 14.6 + M_e(-0.1745 + M_e(0.0083 + M_e(0.3232 + M_e(-0.7061 + 0.3016M_e)))) \text{ if } M_e \leq 1.1 \\ -114.6 + M_e(56.54 - 7.561M_e) \text{ if } 1.1 < M_e \leq 4 \end{cases}$$

$$G(M_e) = \begin{cases} 0 \text{ if } M_e \leq 1.1 \\ 928.12 + M_e(-427.97 + 53.192M_e) \text{ if } 1.1 < M_e \leq 4 \end{cases}$$

B. Gleyzes criterion

The term $\mathcal{B}(H_i)$ of the Gleyzes criterion (Eq. (3)) is:

$$\mathcal{B}(H_i) = \begin{cases} -\dfrac{162.11093}{H_i^{1.1}} & 3.36 < H_i \\ -73 \exp\left(-1.56486(H_i - 3.02)\right) & 2.8 < H_i < 3.36 \\ -103 \exp\left(-4.12633(H_i - 2.8)\right) & H_i < 2.8. \end{cases} \tag{25}$$

C. Integration by means of transport equations

In the following sections, we show that solving Eqs.(17) and (16) corresponds to computing s and $\bar{\Lambda}_2$ by means of transport equations.

1. Transport equation to compute s

Let s be the curvilinear coordinate at $(\underline{x}, t)$. At $t + \Delta t$, the new location is $\underline{x} + \Delta\underline{x} = \underline{x} + \underline{U}\Delta t$ and the curvilinear coordinate is $s(\underline{x} + \Delta\underline{x}, t + \Delta t) = s(\underline{x}, t) + \Delta t\|\underline{U}\|$. A Taylor expansion yields:

$$s(\underline{x} + \Delta\underline{x}, t + \Delta t) \cong s(\underline{x}, t) + \nabla s \cdot \underline{U}\Delta t + \partial_t s\Delta t \tag{26}$$

which implies that:

$$\partial_t s + \nabla s \cdot \underline{U} = \|\underline{U}\|. \tag{27}$$

Combining Eq. (27) with the continuity equation of the Navier-Stokes equation yields:

$$\partial_t(\rho s) + \nabla \cdot (\rho s\underline{U}) = \rho\|\underline{U}\|. \tag{28}$$

2. Transport equation to compute $\bar{\Lambda}_2$

Let $\bar{\Lambda}_2$ be the average Pohlhausen value at $(\underline{x}, t)$. At $t + \Delta t$, the new location is $\underline{x} + \Delta\underline{x} = \underline{x} + \underline{U}\Delta t$ and the average Pohlhausen value is

$$\bar{\Lambda}_2(\underline{x} + \Delta\underline{x}, t + \Delta t) = \frac{s\bar{\Lambda}_2(\underline{x}, t) + \Delta t\|\underline{U}\|\Lambda_2}{s(\underline{x} + \Delta\underline{x}, t + \Delta t)} \tag{29}$$

.

A Taylor expansion yields:

$$\bar{\Lambda}_2(\underline{x}, t) + \nabla\bar{\Lambda}_2 \cdot \underline{U}\Delta t + \partial_t\bar{\Lambda}_2\Delta t \cong \frac{s\bar{\Lambda}_2(\underline{x}, t) + \Delta t\|\underline{U}\|\Lambda_2}{s(\underline{x}, t) + \nabla s \cdot \underline{U}\Delta t + \partial_t s\Delta t} \tag{30}$$

which can be combined with Eq. (27):

$$\left(\bar{\Lambda}_2(\underline{x}, t) + \nabla\bar{\Lambda}_2 \cdot \underline{U}\Delta t + \partial_t\bar{\Lambda}_2\Delta t\right)\left(s(\underline{x}, t) + \Delta t\|\underline{U}\|\right) = s\bar{\Lambda}_2(\underline{x}, t) + \Delta t\|\underline{U}\|\Lambda_2 \tag{31}$$

Neglecting $O(\Delta t^2)$ terms yields:

$$\partial_t\bar{\Lambda}_2 + \nabla\bar{\Lambda}_2 \cdot \underline{U} = \frac{\|\underline{U}\|}{s}\left(\Lambda_2 - \bar{\Lambda}_2\right). \tag{32}$$

Combining Eq. (32) with the continuity equation of the Navier-Stokes equation yields:

$$\partial_t(\rho\bar{\Lambda}_2) + \nabla \cdot (\rho\bar{\Lambda}_2\underline{U}) = \rho\frac{\|\underline{U}\|}{s}\left(\Lambda_2 - \bar{\Lambda}_2\right). \tag{33}$$

References

[1] Langtry, R. B., and Menter, F. R., "Correlation-Based Transition Modeling for Unstructured Parallelized Computational Fluid Dynamics Codes," *AIAA Journal*, Vol. 47, No. 12, 2009, p. 2894–2906. doi:https://doi.org/10.2514/1.42362.

[2] Langtry, R., Sengupta, K., Yeh, D., and Dorgan, A., "Extending the γ-$Re_{\theta t}$ Correlation based Transition Model for Crossflow Effects," *45th AIAA Fluid Dynamics Conference*, American Institute of Aeronautics and Astronautics, 2015, pp. 1–12. doi: https://doi.org/10.2514/6.2015-2474.

[3] Grabe, C., Shengyang, N., and Krumbein, A., "Transport Modeling for the Prediction of Crossflow Transition," *AIAA Journal*, Vol. 56, No. 8, 2018, pp. 3167–3178. doi:https://doi.org/10.2514/1.J056200.

[4] Coder, J. G., and Maughmer, M. D., "Computational Fluid Dynamics Compatible Transition Modeling Using an Amplification Factor Transport Equation," *AIAA Journal*, Vol. 52, No. 11, 2014, p. 2506–2512. doi:https://doi.org/10.2514/1.J052905.

[5] Van Ingen, J. L., "A suggested semi-empirical method for the calculation of the boundary layer transition region," Tech. Rep. VTH-74, Dept. of Aerospace Engineering, Delft Univ. of Technology, 1956.

[6] Smith, A. M. O., and Gamberoni, N., "Transition, pressure gradient, and stability theory," Tech. Rep. ES-26388, Douglas Aircraft, 1956.

[7] Drela, M., and Giles, M. B., "Viscous-inviscid analysis of transonic and low Reynolds number airfoils," *AIAA journal*, Vol. 25, No. 10, 1987, pp. 1347–1355. doi:https://doi.org/10.2514/3.9789.

[8] Coder, J. G., "Enhancement of the Amplification Factor Transport Transition Modeling Framework," *55th AIAA Aerospace Sciences Meeting*, American Institute of Aeronautics and Astronautics, 2017, pp. 1–14. doi:https://doi.org/10.2514/6.2017-1709.

[9] Xu, J., Han, X., Qiao, L., Bai, J., and Zhang, Y., "Fully Local Amplification Factor Transport Equation for Stationary Crossflow Instabilities," *AIAA Journal*, 2019, pp. 1–12. doi:https://doi.org/10.2514/1.J057502.

[10] Stock, H. W., and Haase, W., "Determination of length scales in algebraic turbulence models for Navier-Stokes methods," *AIAA Journal*, Vol. 27, No. 1, 1989, pp. 5–14. doi:https://arc.aiaa.org/doi/abs/10.2514/3.10087.

[11] Stock, H. W., and Haase, W., "Feasibility Study of eN Transition Prediction in Navier-Stokes Methods for Airfoils," *AIAA Journal*, Vol. 37, No. 10, 1999, pp. 1187–1196. doi:https://arc.aiaa.org/doi/10.2514/2.612.

[12] Cliquet, J., Houdeville, R., and Arnal, D., "Application of Laminar-Turbulent Transition Criteria in Navier-Stokes Computations," *AIAA Journal*, Vol. 46, No. 5, 2008, pp. 1182–1190. doi:https://doi.org/10.2514/1.30215.

[13] Bégou, G., Deniau, H., Vermeersch, O., and Casalis, G., "Database Approach for Laminar-Turbulent Transition Prediction: Navier–Stokes Compatible Reformulation," *AIAA Journal*, 2017, pp. 3648–3660. doi:https://doi.org/10.2514/1.J056018.

[14] Pascal, L., Delattre, G., Deniau, H., Bégou, G., and Cliquet, J., "Implementation of stability-based transition models by means of transport equations," *AIAA Aviation 2019 Forum*, American Institute of Aeronautics and Astronautics, 2019, pp. 1–12. doi:https://doi.org/10.2514/6.2019-3323.

[15] Ströer, P., Krimmelbein, N., Krumbein, A., and Grabe, C., "Stability-Based Transition Transport Modeling for Unstructured Computational Fluid Dynamics Including Convection Effects," *AIAA Journal*, 2020, pp. 1–12. URL https://arc.aiaa.org/doi/10.2514/1.J058762.

[16] Ströer, P., Krimmelbein, N., Krumbein, A., and Grabe, C., "Stability Based Transition Transport Modeling for Unstructured Computational Fluid Dynamics Under Transonic Flow Conditions," *AIAA Scitech 2020 Forum*, American Institute of Aeronautics and Astronautics, 2020, pp. 1–15. URL https://arc.aiaa.org/doi/abs/10.2514/6.2020-0564.

[17] Arnal, D., Casalis, G., and Houdeville, R., "Practical transition prediction methods: subsonic and transonic flows," *VKI Lectures Series Advances in Laminar-Turbulent Transition Modelling*, 2008.

[18] Gleyzes, C., Cousteix, J., and Bonnet, J. L., "Theoretical and experimental study of low Reynolds number transitional separation bubbles," *Conference on Low Reynolds Number Airfoil Aerodynamics, Notre Dame, IN*, 1985, pp. 137–152.

[19] Arnal, D., Habiballah, M., and Coustols, E., "Théorie de l'instabilité laminaire et critères de transition en écoulement bi et tridimensionnel," *La Recherche Aérospatiale*, Vol. 2, 1984, pp. 125–143.

[20] Arnal, D., Houdeville, R., Séraudie, A., and Vermeersch, O., "Overview of laminar-turbulent transition investigations at ONERA toulouse," *41st AIAA Fluid Fynamics Conference*, 2011, pp. 1–13. doi:https://doi.org/10.2514/6.2011-3074.

[21] Perraud, J., and Durant, A., "Stability-Based Mach Zero to Four Longitudinal Transition Prediction Criterion," *Journal of Spacecraft and Rockets*, 2016, pp. 730–742. doi:https://doi.org/10.2514/1.A33475.

[22] Hue, D., Vermeersch, O., Duchemin, J., Colin, O., and Tran, D., "Wind-Tunnel and CFD Investigations Focused on Transition and Performance Predictions of Laminar Wings," *AIAA Journal*, Vol. 56, No. 1, 2018, pp. 132–145. doi:https://doi.org/10.2514/1.J056088.

[23] Hue, D., Vermeersch, O., Bailly, D., Brunet, V., and Forte, M., "Experimental and Numerical Methods for Transition and Drag Predictions of Laminar Airfoils," *AIAA Journal*, Vol. 53, No. 9, 2015, pp. 2694–2712. doi:https://doi.org/10.2514/1.J053788.

[24] Bernardos, L. F., Richez, F., and Gleize, V., "RANS modeling of Laminar Separation Bubbles around Airfoils at Low Reynolds conditions," *AIAA Aviation 2019 Forum*, American Institute of Aeronautics and Astronautics, 2019, pp. 1–20. doi:https://doi.org/10.2514/6.2019-2922.

[25] Gross, R., Courty, J.-C., Tran, D., Mallet, M., Arnal, D., Vermeersch, O., and Hue, D., "Prediction of laminar/turbulent transition in an unstructured finite element Navier Stokes solver using a boundary layer code with emphasis on cross flow transition," *3AF 50th International Conference on Applied Aerodynamics*, 2015, pp. 1–10.

[26] Perraud, J., Arnal, D., Casalis, G., Archambaud, J.-P., and Donelli, R., "Automatic transition predictions using simplified methods," *AIAA journal*, Vol. 47, No. 11, 2009, pp. 2676–2684. doi:https://doi.org/10.2514/1.42990.

[27] Kenwright, D. N., Henze, C., and Levit, C., "Feature extraction of separation and attachment lines," *Visualization and Computer Graphics, IEEE Transactions on visualization and computer graphics*, Vol. 5, No. 2, 1999, pp. 135–144. doi: https://doi.org/10.1109/2945.773805.

[28] Bégou, G., "Prevision de la transition laminaire-turbulent dans le code elsA par la méthode des paraboles," Ph.D. thesis, Université de Toulouse, 2018.

[29] Stock, H. W., and Haase, W., "Navier-Stokes Airfoil Computations with eN Transition Prediction Including Transitional Flow Regions," *AIAA journal*, Vol. 38, No. 11, 2000, pp. 2059–2066. doi:https://doi.org/10.2514/2.893.

[30] Spalart, P., and Allmaras, S. R., "A One-Equation Turbulence Model for Aerodynamic Flows," *AIAA*, Vol. 439, No. 1, 1992. doi:https://doi.org/10.2514/6.1992-439.

[31] Menter, F. R., "Two-equation eddy-viscosity turbulence models for engineering applications," *AIAA journal*, Vol. 32, No. 8, 1994, pp. 1598–1605. doi:https://doi.org/10.2514/3.12149.

[32] Cambier, L., Heib, S., and Plot, S., "The Onera elsA CFD software: input from research and feedback from industry," *Mechanics & Industry*, Vol. 14, No. 3, 2013, pp. 159–174. doi:https://doi.org/10.1051/meca/2013056.

[33] Perraud, J., Vermeersch, O., and Houdeville, R., "Descriptif et mode d'emploi du code 3C3D V5.4.8," Tech. Rep. RT 1/18325 DMAE, ONERA, 2011.

[34] Kruse, M., Munoz, F., and Radespiel, R., "Transition Prediction Results for Sickle Wing and NLF(1)-0416 Test Cases," *2018 AIAA Aerospace Sciences Meeting*, American Institute of Aeronautics and Astronautics, 2018, pp. 1–14. doi:https: //doi.org/10.2514/6.2018-0537.

[35] Mack, L. M., "Transition prediction and linear stability theory," *AGARD Conference Proceedings*, 1977, pp. 1.1–1.22.

[36] Perraud, J., Deniau, H., and Casalis, G., "Overview of transition prediction tools in the elsA software," *ECCOMAS*, 2014, pp. 1–20.

[37] Petzold, R., and Radespiel, R., "Transition on a Wing with Spanwise Varying Crossflow and Linear Stability Analysis," *AIAA Journal*, Vol. 53, No. 2, 2015, pp. 321–335. doi:https://doi.org/10.2514/1.J053127.

[38] Habiballah, M., "Analyse de l'instabilité des couches limites laminaires et prévision de la transition du régime laminaire au régime turbulent," Ph.D. thesis, École Nationale Supérieure de l'Aéronautique et de l'Espace, 1981.